JGR Atmospheres

RESEARCH ARTICLE
10.1029/2025JD045060

The Reflectance Distribution of Shallow Cumulus and Its Environs From High Spatial Resolution ASTER Images

Mengqi Liu[1,2], **Ákos Horváth**[2], **Stefan A. Buehler**[2], **Xiangao Xia**[3,4], and **Mirjana Sakradzija**[5]

[1]Key Laboratory of Atmospheric Sounding, Chengdu University of Information Technology, Chengdu, China, [2]Meteorological Institute, University of Hamburg, Hamburg, Germany, [3]LAGEO, Institute of Atmospheric Physics, Chinese Academy of Sciences, Beijing, China, [4]University of Chinese Academy of Sciences, Beijing, China, [5]Department of Geography, Ludwig-Maximilians Universität, München, Germany

Key Points:

- We investigate the reflectance distribution of shallow cumulus as a function of cloud size using high-resolution satellite observations
- Independent of cloud size, reflectance increases by 20%–25% above its clear-sky value within one chord length of the cloud edge
- Small clouds have larger transition zones relative to their size, as absolute transition zone size does not scale linearly with cloud size

Supporting Information:

Supporting Information may be found in the online version of this article.

Correspondence to:

M. Liu,
liumq@cuit.edu.cn

Citation:

Liu, M., Horváth, Á., Buehler, S. A., Xia, X., & Sakradzija, M. (2026). The reflectance distribution of shallow cumulus and its environs from high spatial resolution ASTER images. *Journal of Geophysical Research: Atmospheres*, *131*, e2025JD045060. https://doi.org/10.1029/2025JD045060

Received 3 AUG 2025
Accepted 14 JAN 2026

Author Contributions:

Conceptualization: Xiangao Xia
Data curation: Mengqi Liu
Investigation: Mengqi Liu
Methodology: Mengqi Liu, Ákos Horváth
Supervision: Ákos Horváth, Stefan A. Buehler, Xiangao Xia, Mirjana Sakradzija
Writing – original draft: Mengqi Liu
Writing – review & editing: Ákos Horváth, Stefan A. Buehler, Xiangao Xia, Mirjana Sakradzija

Abstract We investigate the 1D reflectance distribution of shallow cumulus as a function of cloud size, using high-spatial-resolution observations from the Advanced Spaceborne Thermal Emission and Reflection Radiometer (ASTER). Reflectance transects through clouds are compared between Inner Mongolia and Tropical Ocean. The reflectance shows varying degrees of shadowing–illumination effects, depending on transect direction. Perpendicular to the solar azimuth (cross-sun direction), where shadowing–illumination effects are minimal, the reflectance follows a symmetric, bell-shaped decrease from the cloud center to the cloud edge and into the transition zone or radiative halo. The peak reflectance is located slightly off-center for larger clouds, which can be explained by the competition between radiative smoothing and sharpening. Reflectance steadily increases with cloud size in both regions; however, Inner Mongolia clouds are significantly brighter and have larger cloud top height variations for the same chord length (cloud diameter). The size and height of continental clouds also systematically increase with surface temperature, indicating more vigorous convection over warm, dry land characterized by high Bowen ratio. In the halo region, reflectance increases by 20%–25% above its clear-sky value within one chord length of the cloud edge, the brightness enhancement showing little variation with cloud size. The chord-length normalized size of the halo steadily decreases with cloud size, as the absolute halo size does not scale linearly with cloud size. This observation, consistent with large-eddy simulations of the moist buffer around shallow cumulus, suggests that the processes responsible for halo formation have size-independent length scales.

Plain Language Summary Shallow cumulus, consisting mainly of clouds smaller than 1 km, are frequently observed over many continental and oceanic regions of the world. Using 15 m-resolution satellite products, we studied the reflectance distribution through shallow cumulus in the Inner Mongolia and Tropical Ocean region. First, reflectance distribution along different directions was compared to see the influence of the sun's position. The cross-sun direction was chosen to compare the reflectance distribution of shallow cumulus on continental and oceanic surface, which show an obvious size-dependence pattern. Furthermore, we investigated and validated the relationship between the cloud size and the relative and absolute size of the "halo" around shallow cumulus.

1. Introduction

It is well-established by now that the thermodynamic, dynamic, and radiative properties of the cloudy atmosphere gradually transition into those of the cloud-free atmosphere. Both in modeling and observational practice, however, the atmospheric continuum is discretized into distinct "cloudy" and "clear" regimes by thresholding a relevant quantity, such as condensed water content or reflectance. This dichotomy neglects the variation of atmospheric properties between the clear-sky and in-cloud environments, which is particularly troublesome in broken cloud fields comprising scattered clouds and clear gaps (Charlson et al., 2007). The regime between completely clear and fully cloudy states has previously been investigated using airborne, ground-based, and satellite observations as well as Large Eddy Simulations (LES) and is variously called the "humidity halo" (Perry & Hobbs, 1996; Radke & Hobbs, 1991), "transition zone" (Perry & Hobbs, 1996; Várnai & Marshak, 2009, 2011), "twilight zone" (Koren et al., 2007), or "moist buffering halo" (Gu et al., 2021, 2024). The different names reflect the different metrics used for quantifying the transition regime.

Aircraft transects across isolated small cumulus clouds (Cu) analyzed by Radke and Hobbs (1991) and Perry and Hobbs (1996) showed enhanced humidity regions surrounding the clouds, which can extend for a few cloud radii. The humidity halo coincided with enhanced turbulence and increased particle concentrations. Koren et al. (2007) investigated the "twilight zone" using a few marine cloud scenes from the Moderate Resolution Imaging Spectroradiometer (MODIS) and years of ground-based Sun photometer data from the Aerosol Robotic Network (AERONET). They found that the mean clear-sky reflectance as well as the retrieved aerosol optical depth and particle size systematically increased with decreasing distance to the nearest cloud. Twohy et al. (2009) combined in situ aircraft measurements of relative humidity (RH) with scattering observations in the vicinity of two small marine trade Cu. The RH showed a sharp increase within 1–2 km from the cloud edge. The corresponding solar reflectance measured by the Multichannel Cloud Radiometer rose by 40%–80%, which could be largely explained by the increased scattering cross section of the local marine aerosol mixture as it underwent hygroscopic growth in the elevated humidity of the near-cloud environment.

Although aerosol swelling is an important factor, Várnai and Marshak (2009) demonstrated that three-dimensional (3D) radiative effects also measurably contribute to the brightness enhancement in the transition zone. By analyzing a large set of MODIS imagery of low-level clouds in the North Atlantic Ocean, they found that the reflectance enhancement can extend up to 15 km away from cloud edge and it is stronger near illuminated cloud sides than near shadowed ones; an asymmetry, which implies 3D radiative effects. Later studies employing the spaceborne Cloud-Aerosol Lidar with Orthogonal Polarization (CALIOP), however, reaffirmed the importance of changing aerosol particle size and optical properties in the emergence of the brightness halo around clouds. Tackett and Di Girolamo (2009) and Várnai and Marshak (2011) analyzed CALIOP clear-sky backscatter and color ratio observations, which are unaffected by 3D radiative effects. They found that both the attenuated backscatter and the color ratio systematically increase toward clouds, indicating enlarged particle sizes due to aerosol humidification and new particle production by cloud detrainment.

From the numerous prior studies, the following picture thus emerges about the near-cloud environment. In remote sensing observations, the transition zone manifests itself as systematically increasing brightness or backscatter when moving toward clouds. The observed reflectance enhancement is the result of a combination of factors: (a) hygroscopic growth of aerosol particles and the corresponding increase in their scattering coefficient, (b) increased particle formation near clouds, (c) 3D radiative effects, and (d) presence of undetectable clouds. The relative contributions of the various factors, however, remains unquantified.

The binary representation of the transition zone continuum by the distinct categories of "clear" and "cloud" can lead to various errors. It introduces sensor-dependent biases in the retrieval of the micro- and macro-physical properties of aerosols and clouds (Várnai & Marshak, 2009). The local radiative effect of clouds on their surroundings is also substantial, both in the shortwave and longwave, which results in biased estimates of aerosol and cloud radiative forcing (Charlson et al., 2007; Eytan et al., 2025; Mieslinger et al., 2022). Moreover, neglecting the humidity halo in convection parameterizations yields underestimated entrainment rates, which strongly affects the modeled cloud dynamics (Gu et al., 2021, 2024).

Previous satellite studies relying on CALIOP or MODIS data characterized the transition zone at minimum horizontal resolutions ranging from 1/3–1 km; thus, they could not sample small shallow Cu (Koren et al., 2007; Tackett & Di Girolamo, 2009; Várnai & Marshak, 2009, 2011). Twohy et al. (2009) used 30-m-resolution airborne imagery; however, they only observed two Cu cases. In addition, these works investigated marine boundary layer clouds exclusively, although scattered-to-broken cloudiness is common over land too (Shi et al., 2017). The studies exploiting 15-m-resolution imagery from the Advanced Spaceborne Thermal Emission and Reflection Radiometer (ASTER) only investigated the macrophysical properties of shallow Cu, such as size distribution, cloud top height, spatial organization, or cloud fraction (De Vera et al., 2024; Mieslinger et al., 2019, 2022; Zhao & Di Girolamo, 2007).

The CALIOP and MODIS studies, which noted a transition zone of $\mathcal{O}(10\,\mathrm{km})$ wide, analyzed clear-sky reflectance as a function of distance to the nearest cloud, averaged over all cloud types and sizes in mid-latitude or global oceans. They relied on a 1-km resolution cloud mask, which missed a significant portion of small clouds. A direct comparison of MODIS and ASTER images by Zhao and Di Girolamo (2006) found up to a third of "clear" MODIS pixels containing thin, sub-pixel clouds. Undetected clouds lead to the overestimation of the "clear-sky" reflectance and that of the distance to the nearest (detected) cloud, which, in turn, cause an overestimated transition zone width.

Therefore, there is a need to observationally explore the radiative characteristics of the transition zone at smaller scales and for individual cloud types and sizes. This can further help the evaluation of recent high-resolution LES of the shallow Cu moist halo. In particular, the simulations by Gu et al. (2021, 2024) indicated that the normalized size of the moist halo is larger for smaller clouds, while its absolute size does not scale linearly with cloud size. Such halo structure was found for both the oceanic Barbados Oceanographic and Meteorological Experiment (BOMEX) case and the continental Atmospheric Radiation Measurement (ARM) Program, Southern Great Plains (SGP) case.

In our work, we characterize the reflectance distribution inside and outside shallow Cu as a function of cloud size using high-resolution ASTER images. The use of ASTER data with a horizontal resolution comparable to that of the LES, allows exploring small clouds with chord lengths down to 90 m. Unlike earlier studies, the analysis is done not only over ocean, but also over land areas in Inner Mongolia. We first analyze composited reflectance distributions along cloud chords in different azimuth directions, then compare the characteristics of the observed brightness halo, including its dependence on shallow Cu size, with those of the LES moist halo. Similarly to Gu et al. (2021, 2024), we focus on the immediate environment of clouds within a couple of chord lengths of the cloud edge, rather than on the far-field as in previous satellite studies.

The paper is organized as follows. Section 2 describes the ASTER imagery, the cloud mask, and the compositing algorithm. Section 3 presents the observed reflectance of shallow Cu and its transition zone as a function of cloud size. Finally, a discussion and summary are given in Section 4.

2. Materials and Methods

2.1. ASTER Imagery

ASTER flies aboard Terra, a polar-orbiting satellite in a Sun-synchronous orbit with an equator crossing time of 10:30 local solar time. ASTER consists of one nadir and one backward-pointing camera. The nadir camera, whose images are used in this study, has three separate radiometers. The visible and near-infrared sensor covers the wavelength range 0.53–0.86 μm in three bands with 15-m spatial resolution. The shortwave infrared (SWIR) radiometer consists of six bands in the range of 1.60–2.43 μm with 30-m resolution, and the thermal infrared (TIR) radiometer comprises five bands covering 8.13–11.65 μm with 90-m spatial resolution (Abrams et al., 2000; Yamaguchi et al., 1998). Data are available in 60×60 km^2 scenes, each corresponding to 9 s of observation time. ASTER's on-request image acquisition prioritizes cloud-free scenes for mapping and disaster monitoring; therefore, the temporal sampling frequency is irregular and varies with geographic region.

Inner Mongolia (IM) grassland is an ideal region for the study of continental shallow cumulus, because of its flat terrain, uniform vegetation, and high frequency of shallow cumulus in summer (Shi et al., 2017). The study area in Inner Mongolia is limited to 41°–47°N and 110°–120.5°E (Figure 1a), zonally covering the central part of Inner Mongolia, where the vegetation is dominated by grass in summer (June-July-August). We filter all available images between 2002 and 2022 for pure shallow cumulus cloud fields by visual inspection. Scenes partially dominated by stratocumulus probably indicate heterogeneous meteorological conditions and, thus, are eliminated. Scenes with cirrus over shallow cumulus are also excluded. Our IM data set consists of 233 carefully selected and visually checked ASTER images of summertime shallow cumulus. The number of scenes in June, July, and August are 74, 76, and 83, respectively.

We also selected similarly filtered shallow cumulus scenes over the Tropical Ocean (TO) from the data set of Mieslinger et al. (2019), covering the Northern Hemisphere from 0° to 23.5°N (Figure 1b), to compare the reflectance distributions over land and sea. The 194 marine shallow cumulus scenes are from the summer months of 2001–2006, with 68, 42, and 84 scenes from June, July, and August, respectively. All used ASTER files are listed in Text S1 in Supporting Information S1.

2.2. Methods

2.2.1. Cloud Detection

ASTER does not have operational cloud products; thus, the cloud mask must be derived independently. Previous ASTER cloud detection schemes focused on the ocean surface (De Vera et al., 2024; Hulley & Hook, 2008; Mieslinger et al., 2019; Werner et al., 2016; Zhao & Di Girolamo, 2007). Due to the low albedo of the ocean, these

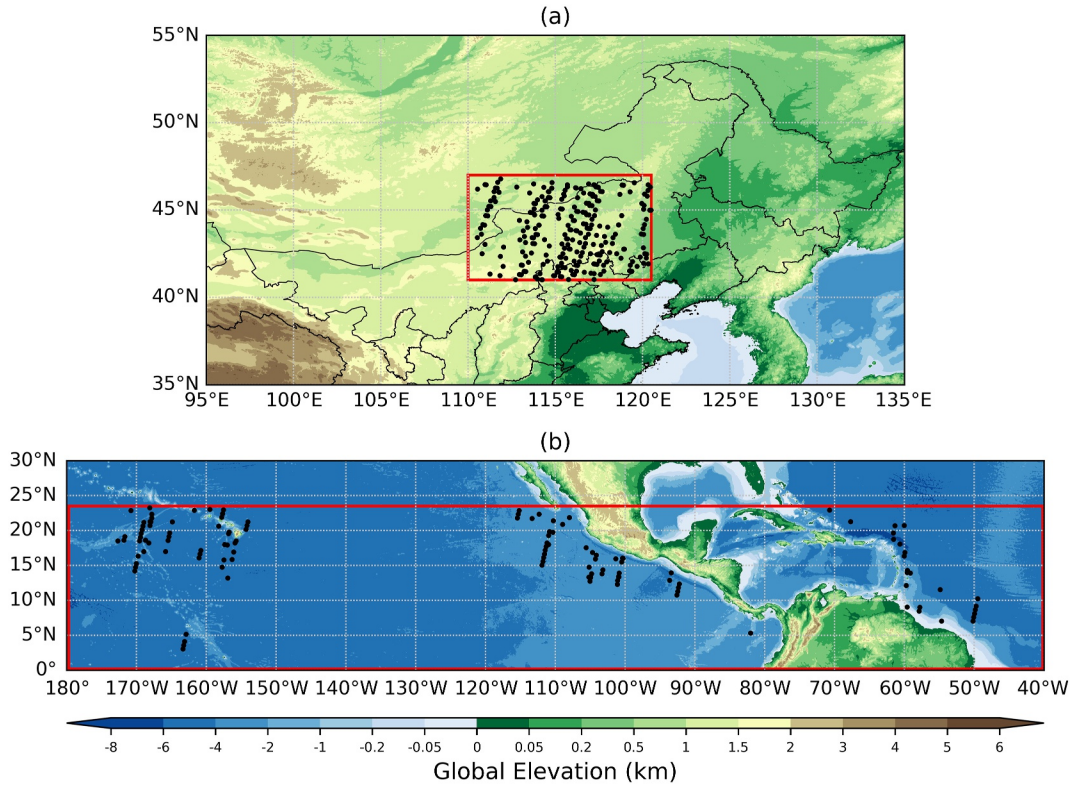

Figure 1. The geographical location (black dots) of the ASTER shallow cumulus images over a Digital Elevation Map in the (a) Inner Mongolia and (b) Tropical Ocean domain (red box).

schemes use relatively low reflectance thresholds to detect clouds, which would overestimate cloud cover over brighter land surfaces. Therefore, we implement a new cloud detection algorithm for ASTER land scenes, using thresholds adjusted to the observed reflectance of grassland from Govender et al. (2007). This algorithm employs three tests and classifies each 15 m pixel as clear or cloudy. Two tests are based on reflectivity (R) thresholds in the red band ($R_2 > 0.23$ in the 0.66-μm band 2) and the near-infrared band ($R_{3N} > 0.33$ in the 0.82-μm band 3N), which are designed to distinguish bright clouds from dark land surface. An additional threshold of 300 K is applied to the 10.6-μm band 13 brightness temperatures to eliminate warm surface features (Hulley & Hook, 2008).

Figure 2 shows a typical shallow cumulus scene in Inner Mongolia. The false-color image in Figure 2a exemplifies the information content of the visible bands, while Figure 2b shows the corresponding cloud mask. The performance of the new cloud detection algorithm was visually verified for all land scenes. The cloud fraction in individual land images ranges from 0.01 to 0.46 with an average of 0.17% and 85% of the images have a cloud fraction less than 0.25.

For the ocean surface, we used the ASTER cloud mask from Mieslinger et al. (2019). This algorithm employs five threshold tests and classifies each 15-m pixel as clear, probably clear, probably cloudy, or cloudy. Four tests are based on thresholding the near-infrared (0.82-μm band 3N) and shortwave-infrared (2.1-μm band 5) reflectivities, as well as the green (0.56-μm) to red (band 1/band 2) and near-infrared to red (band 3N/band 2) reflectance ratios, designed to detect clouds (Werner et al., 2016). An additional test based on band 14 (11.65 μm) is applied to correct warm ocean pixels that are labeled cloudy after the first four tests. Finally, the clear and probably clear, as well as the cloudy and probably cloudy classes are merged to form a binary (clear/cloudy) mask. Figures 2c and 2d show a typical marine shallow cumulus scene and its cloud mask over the Atlantic Ocean. In oceanic scenes, cloud fraction ranges between 0.01 and 0.46 with an average of 0.13% and 80% of the images have a cloud fraction below 0.17.

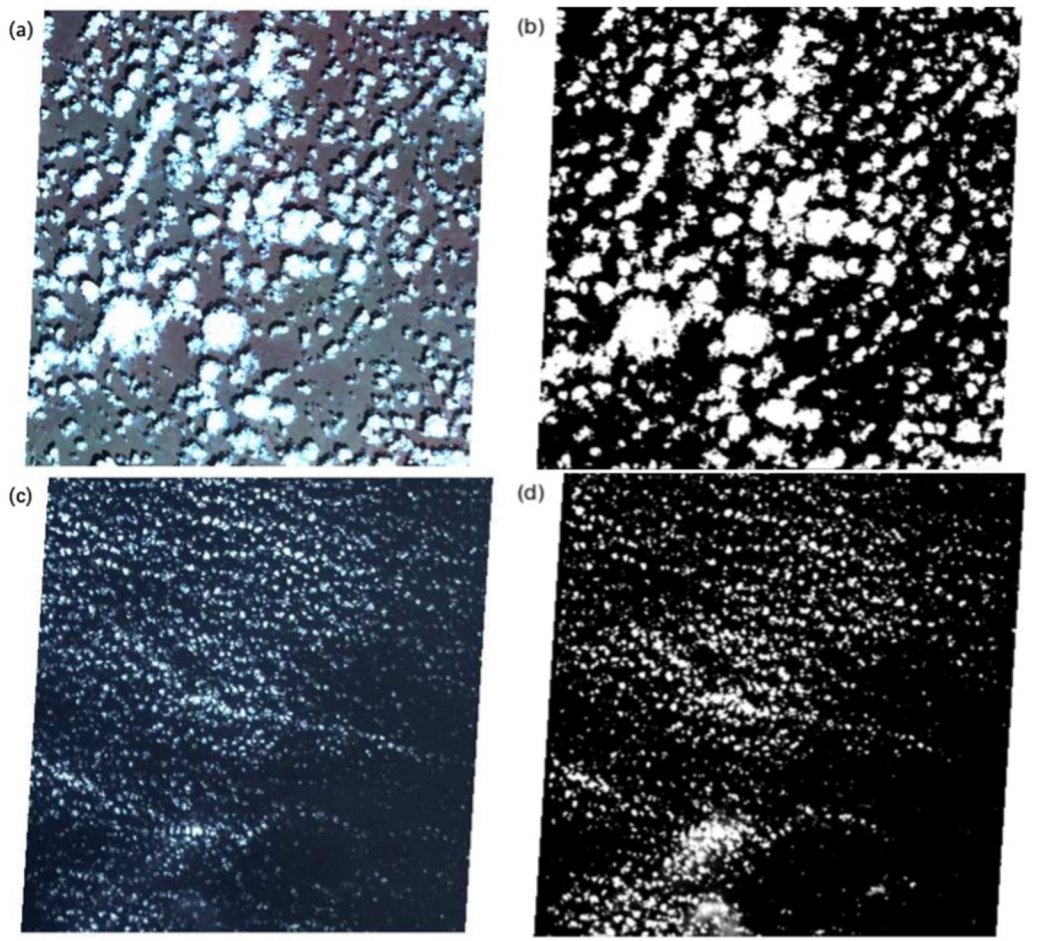

Figure 2. False-color ASTER scenes and cloud detection results in (a, b) Inner Mongolia on 19 June 2002 at 03:35:18 UTC and (c, d) Tropical Ocean on 6 July 2005 at 17:17:21 UTC. In the cloud mask, white represents cloud and black represents clear.

Note that the lower resolution SWIR and TIR bands are resampled to the 15-m grid of band 3N by nearest-neighbor interpolation. Nevertheless, the cloud mask retains an essentially 15-m resolution, because it depends predominantly on band 3N, while the SWIR and TIR tests are triggered only occasionally. Similar to Hulley and Hook (2008), Werner et al. (2016), and Mieslinger et al. (2019), our cloud detection uses fixed reflectance thresholds which are independent of solar zenith angle (SZA). Mieslinger et al. (2019) evaluated the performance of such a cloud mask against the reference cloud mask of Zhao and Di Girolamo (2007), which uses SZA-dependent thresholds. They found that the obtained cloud field properties (cloud fraction, size distribution, fractal dimension) agreed well with those of Zhao and Di Girolamo (2007), confirming that our cloud masks adequately detect clouds. For identifying individual cloud objects, we followed the four-connectedness rule as in Mieslinger et al. (2019) and De Vera et al. (2024): neighboring cloudy pixels sharing one edge are grouped together, but cloudy pixels sharing only a corner are treated as separate clouds. Single-pixel clouds are excluded from the analysis to reduce noise.

It is important to note that defining clouds by reflectance thresholding, as done in all satellite studies, is directly analogous to thresholding droplet number concentration in aircraft measurements (Perry & Hobbs, 1996; Twohy et al., 2009) or liquid water mixing ratio in LES (Gu et al., 2021, 2024). The cloud size and the location of the cloud–clear interface are somewhat sensitive to the choice of the threshold value, regardless of the analyzed parameter. Due to this unavoidable uncertainty, the qualitative features of the transition zone presented below are more robust than the quantitative ones.

2.2.2. Reflectance Compositing

Our reflectance compositing algorithm is essentially the same as the one used by Gu et al. (2021) to obtain the composited one-dimensional (1-D) structure of thermodynamic and dynamic properties of simulated shallow Cu fields. The thermodynamic variables considered by Gu et al. (2021) were RH, potential temperature, virtual potential temperature, and cloud liquid water, while the dynamic variables were turbulent kinetic energy, horizontal turbulent kinetic energy, and vertical velocity.

Because passive satellite observations cannot provide high-resolution profiles of any of these variables, particularly in the complex environment of broken clouds, to analyze potential environmental gradients from the cloud center to its surrounding regions, here we use the band 3N (0.82 μm) and band 5 (2.16 μm) solar reflectances as proxy for the modeled humidity halo. These two channels are also used in the classic bi-spectral method to retrieve cloud optical thickness and drop effective radius (Werner et al., 2016), although we do not attempt such retrievals in our study. Additionally, band 14 (12 μm) brightness temperatures (BT_{14}), which are the least affected by water vapor absorption among the ASTER BTs, serve as a qualitative proxy for cloud top height (CTH) over the opaque central cloud regions. For opaque clouds, a first-order CTH estimate can be obtained by taking the difference between the surface temperature and the cloud top BT_{14}, and assuming a lapse rate of ≈9 K/km in IM (Shi et al., 2017) and ≈3–4 K/km in TO (Baum et al., 2012). As noted before, the band 5 reflectance and BT_{14} are resampled to the 15-m grid of band 3N by nearest-neighbor interpolation. Therefore, the band 5 and especially the band 14 composites are less smooth–have lower effective resolution–than the band 3N composites.

A schematic of the compositing algorithm is given in Figure 3. For each identified cloud, four lines through the cloud centroid (geometric center) along different directions are taken as 1-D sample slices of the reflectance distribution. We considered the following directions: west–east (W–E), north–south (N–S), the solar principal plane along the solar azimuth angle (SAA or "along-sun"), and the direction perpendicular to SAA (SAA-90 or "cross-sun"). The linear extent of the cloud along a particular line, called the chord length, is used to characterize cloud size.

For each slice, distances are measured from the center of the chord, marked by C, and are normalized by the length of the chord (L, in m). Note that L may vary with direction for a given cloud, indicating non-circular shapes, especially in windy environments. To characterize the reflectance distribution of clouds and their immediate vicinity, the slice is extended from the centroid outward to distances of ±1.5 L (or up to ±2 L for a subset of clouds, see Appendix A). The cloud is between ±0.5 L and the near-field transition zone on the two sides of the cloud is located between −0.5 L and −1.5 L and +0.5 L to +1.5 L. The horizontal range of ±1.5 L is chosen for direct comparability with Gu et al. (2021). It is a reasonable range, considering that most humidity halos found by in situ aircraft measurements had a size less than 1.1 L (Perry & Hobbs, 1996; Twohy et al., 2009), although it does not always capture the full extent of the transition zone.

Use of cloud chords in the W–E and N–S directions of the numerical grid is convenient in modeling studies, where the position of the sun has a negligible effect on the analyzed variables (Griewank et al., 2020; Gu et al., 2021; Guillaume et al., 2018). For satellite observations of solar reflectance, however, the sun's position is of crucial importance. The sunlit side of a non-plane-parallel cloud receives more solar illumination than the shadowy one and tends to appear brighter. Therefore, the along-sun direction (SAA) and the cross-sun direction (SAA-90) represent a more natural coordinate system for the study of reflectance. The along-sun axis maximizes the reflectance asymmetry due to illumination and shadowing, while reflectance along the cross-sun axis is the least affected by the sun's position (Várnai, 2000). The W–E and the N–S directions are subject to various degrees of shadowing depending on the solar azimuth and zenith angle of the scene.

We present results for all four directions, however, the focus is on the cross-sun slice, because this yields the most symmetric reflectance distribution and, thus, is most suitable for characterizing the transition zone with minimal shadowing–illumination effects. The SAA is calculated separately for each ASTER scene, the Sun typically being to the southeast in Inner Mongolia and to the northeast in Tropical Ocean, as depicted in Figures 3a and 3b. The images were acquired at high- to moderate-sun. The solar zenith angle varies between 22° and 39° in IM with a distribution peak at 26° and 75% of the scenes having an SZA between 22° and 32°. In TO, the SZA varies between 15° and 41° with a distribution peak at 20° and 90% of the scenes having an SZA between 15° and 25°.

In all subsequent figures, the variation of reflectance is plotted along the indicated arrows, moving from the tail toward the arrowhead. This choice ensures that the shadowy side is on the left (negative distance values) and the

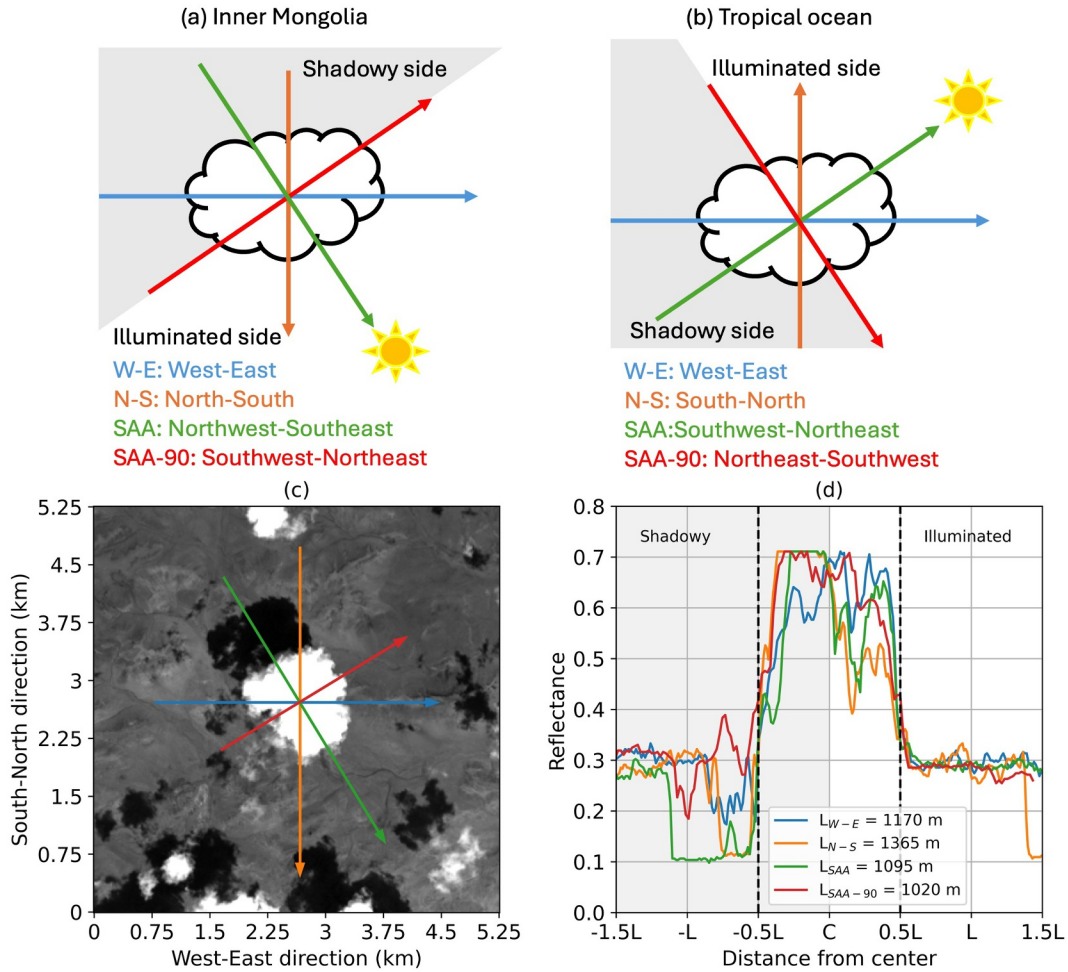

Figure 3. Illustration of the direction of sample slices in (a) Inner Mongolia and (b) Tropical Ocean. Panel (c) depicts a typical cloud in Inner Mongolia (19 June 2002 at 03:35:18 UTC), whose band 3N reflectance distributions along the four indicated directions are shown in panel (d).

illuminated side is on the right (positive distance values) relative to the central cloud object (the shadowy–illuminated distinction is largely reduced for the cross-sun slice). We note that the observed cloud shadow can be shorter or longer than the true stick shadow and can even be completely obscured by other clouds, depending on the sun–satellite geometry (Horváth et al., 2021). Therefore, the "shadowy" side refers to the general area where shadows, if not obscured, can be detected.

Figure 3c shows an example in IM, where shadows cast on the surface are apparent to the north-west of clouds. The band 3N reflectance slices through the central cloud along the four different directions are plotted in Figure 3d. The cloud chord length varies between 1,020 and 1,365 m, depending on direction. Reflectance outside the cloud is generally lower and exhibits larger directional variations on the shadowy side than on the illuminated side, due to the presence of shadows. The along-sun reflectance distribution (green curve) is the most asymmetric. The large drop between −0.6 L and −1.1 L is due to the cloud's self-shadow. The N–S slice (orange curve) is also affected by the self-shadow, but it cuts through a smaller portion of it than the along-sun slice. Reflectance along the W–E direction (blue curve) drops on the shadowy side too; however, this is mostly due to shadows cast by neighboring clouds. The cross-sun slice (red curve) is the least affected by the self-shadow, nevertheless, it can still be affected by shadows of nearby clouds (one of those is apparent at +1 L). In addition to shadows, the spatial variation of land surface reflectance also influences the reflectance distribution. Both of these effects are significantly smaller over the generally dark ocean, but shadowing is still noticeable.

Table 1
The Number of Slices Used for Compositing as a Function of Cloud Chord Length, Direction, and Region

	Inner Mongolia				Tropical Ocean			
Cloud chord length	W–E	N–S	SAA	SAA-90	W–E	N–S	SAA	SAA-90
90 m	40,972	43,754	29,423	6,597	65,407	77,710	45,321	47,386
150 m	11,533	11,695	9,698	2,423	6,122	6,515	4,176	3,633
300 m	470	2,726	2,923	673	1,473	1,512	1,409	1,268
600 m	100	760	924	212	161	137	281	254
900 m	91	579	484	106	305	1,434	469	332

Because individual cases can be noisy, slices from all clouds of a particular chord length along a given direction are averaged to obtain the composited reflectance structure. Gu et al. (2021) binned clouds into three broad size categories in their 25-m resolution simulations: small with $L \leq 160$ m, medium with $160 \text{ m} < L \leq 320$ m, and large with $L > 320$ m. In our analysis of 15-m resolution ASTER data, we show results for five cloud size categories to demonstrate the evolution of reflectance and BT: $L = 90$ m (6 pixels), $L = 150$ m (10 pixels), $L = 300$ m (20 pixels), $L = 600$ m (40 pixels), and $L = 900$ m (60 pixels).

The sample numbers per direction are listed in Table 1, separately for the two study regions. As shown, the number of clouds rapidly decreases with size over both land and ocean, but a factor of 3–6 more small clouds are observed over ocean relative to over land. For all other cloud sizes and directions (especially the cross-sun direction), however, the sample numbers are similar between land and ocean. Note that for a given size bin, the different directions generally sample different cloud populations, due to the variation of chord length with direction in non-circular clouds. Also note that for the largest clouds, there are significantly more N–S chords than W–E chords, because these clouds tend to be formed into elongated shapes by stronger winds. For example, Figure 2a indicates larger, cloud street-like structures that run close to the N–S direction. However, investigating the effects of wind, cloud shape (aspect ratio), and cloud organization is beyond the scope of the current study. Overall, our sample numbers are comparable with those in Gu et al. (2021), which range from a couple of hundred to a few thousand, depending on model altitude.

3. Results

3.1. Overall Reflectance Structure and Dependence on Direction

The composited reflectance and BT_{14} distributions along the four directions are plotted in Figures 4 and 5 for IM and TO, respectively. The curves have a bell shape, with the maximum reflectance and minimum BT_{14} occurring over the optically thickest, highest altitude cloud parts near the centroid, and reflectance gradually decreasing toward the cloud edges and in the transition zone. The BT_{14} increases toward the edges, due partly to lower CTHs but also due to an increasing contribution from the warm surface in the thinner, semitransparent outer cloud parts. As a result of this warm bias, the shape of the BT_{14} curves exaggerates the actual CTH drop between the cloud centroid and the cloud edges, especially for the smaller clouds.

A notable feature in larger clouds ($L \geq 300$ m) is that the peak reflectance tends to be slightly shifted from the cloud centroid, typically toward the illuminated side. For the smallest clouds ($L = 90$ m) in both IM and TO, the reflectance peaks at the cloud center and decreases symmetrically on the shadowy and illuminated sides, both within the cloud and in the transition zone, and along all directions. For larger clouds in IM, however, the peak reflectance is always shifted to the illuminated side in all but the cross-sun direction, with the largest shift occurring in the along-sun direction (e.g., see Figures 4j and 4k for $L = 600$ m). In TO, the reflectance peak is also typically on the illuminated side; however, for the two largest cloud sizes, the peak can be shifted to the shadowy side in certain directions (e.g., see Figures 5j and 5k for $L = 600$ m).

The observed off-center shifts of peak reflectance can be explained by 3D effects, diagnosed in Monte Carlo radiative transfer simulations of synthetic cloud fields as well as in MODIS cloud images (Várnai, 2000; Várnai & Davies, 1999; Várnai & Marshak, 2002). The spatial distribution of shortwave cloud reflectance is influenced primarily by two counteracting 3D mechanisms. Radiative diffusion (horizontal photon transport) constitutes a smoothing effect, which reduces small-scale brightness variations among neighboring cloud pixels. In contrast,

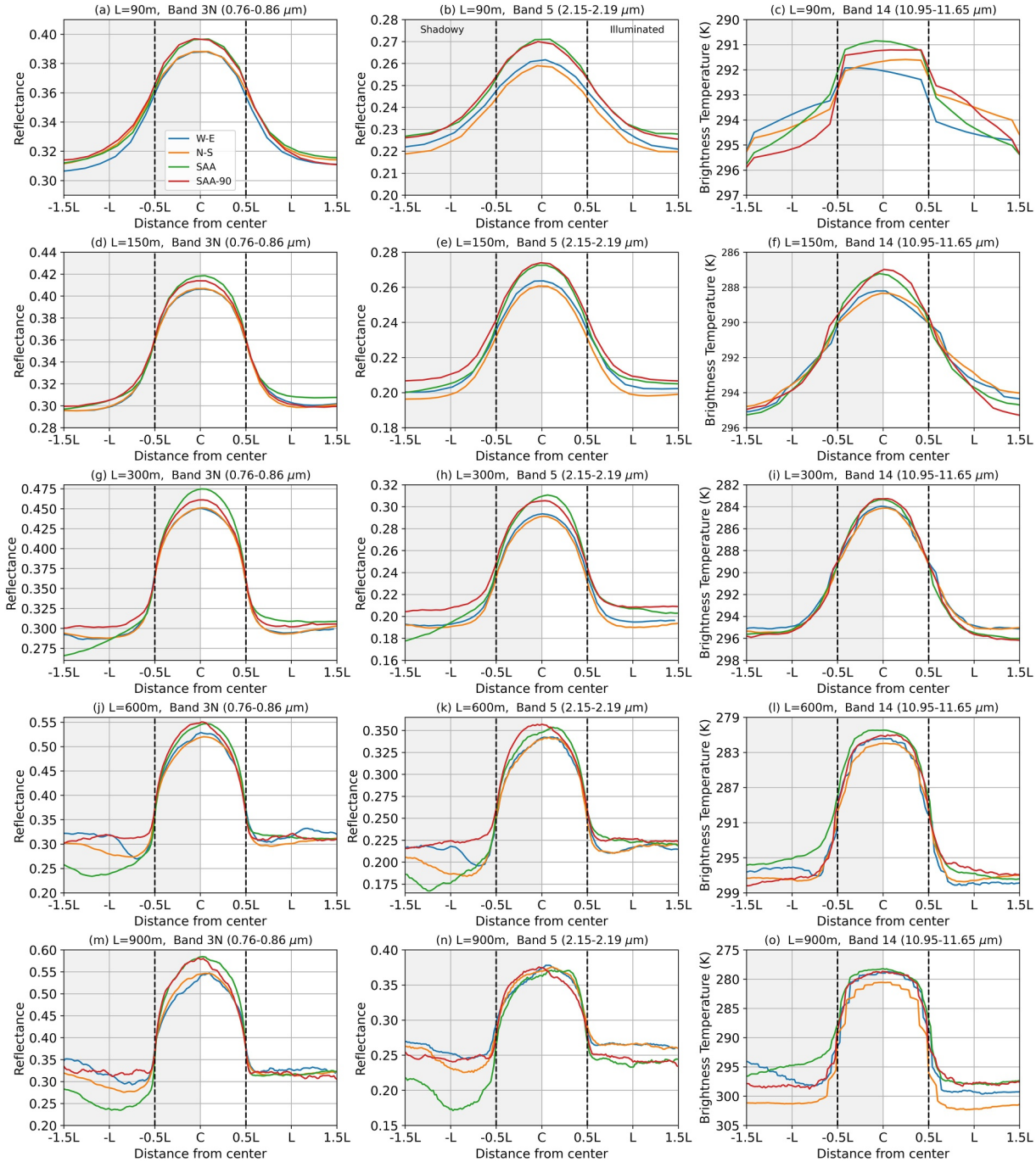

Figure 4. Composited reflectance and BT distributions of shallow cumulus in four directions for a chord length of (a–c) 90 m, (d–f) 150 m, (g–i) 300 m, (j–l) 600 m, and (m–o) 900 m in Inner Mongolia. The gray shading indicates the shadowy side. Note that in the right column, the BT axis is reversed (decreasing) to indicate the general CTH shape. Note the different *y*-axis ranges.

CTH variations introduce a sharpening effect, which enhances brightness variability and shifts the peak reflectance to the illuminated side by thick sun-facing slopes intercepting extra radiation through their sides and casting shadows on the thinner areas behind them. Smoothing dominates when optical thickness variations are due mostly to changes in the volume extinction coefficient (cloud tops are relatively flat). Smoothing becomes more efficient as the average cloud optical thickness increases, because the effect is caused by multiple scattering. Sharpening is strongest in the along-sun direction and weakest in the cross-sun direction, where side illumination–shadowing effects are minimal. Sharpening does not increase with increasing average optical thickness, because it is caused

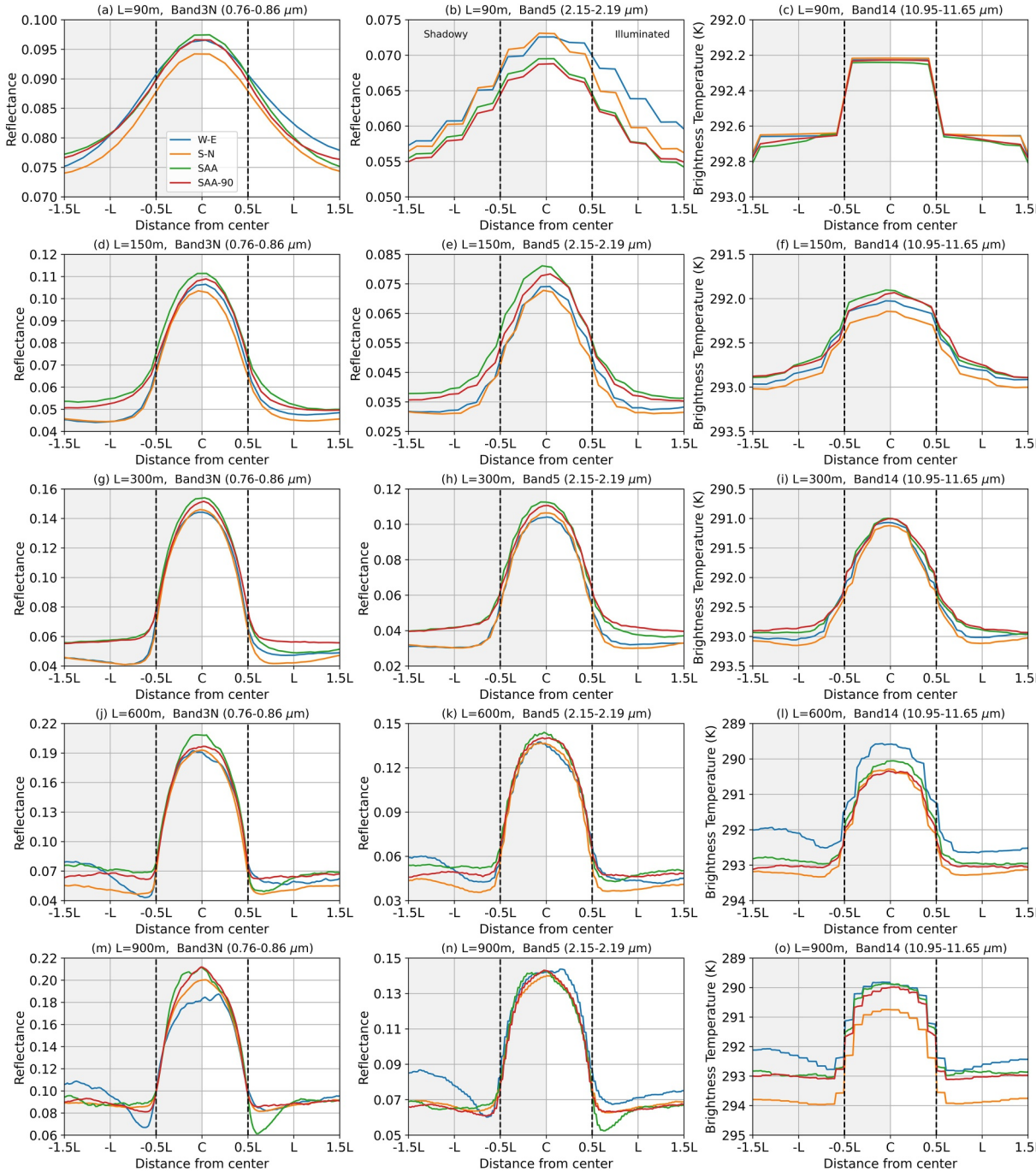

Figure 5. Same as Figure 4 but for the Tropical Ocean region. Note the different *y*-axis ranges.

by low-order scattering; however, the sharpening effect of CTH variations is generally much stronger than the smoothing effect of volume extinction variations (Várnai & Davies, 1999).

The peak reflectance's consistent shift to the illuminated side and the direction dependence of the shift's magnitude indicates the dominance of the sharpening effect in IM clouds. The sharpening effect is also dominant in smaller TO clouds; however, in the horizontally largest and optically thickest clouds, the increasingly efficient smoothing effect can push the peak reflectance slightly to the shadowy side in certain directions (see Figures 5j and 5k). These results suggest that CTH variations are more prominent in continental than in marine shallow Cu. Also note that the composited reflectance is almost always the highest in the along-sun direction, thanks to the

overwhelming influence of the very bright sunlit slopes. The reflectance is typically the second highest in the cross-sun direction due to the minimal presence of in-cloud shadows. Reflectance in the W–E and N–S directions tend to be the smallest, depending on the degree of observed shadows.

In contrast to reflectance, there is no obvious off-center shift in the location of the coldest cloud point and the magnitude of BT_{14} does not show the same systematic direction dependence. The slight asymmetry within the smallest IM clouds (L = 90 m or L = 150 m) arises because these clouds fall into one or at most two adjacent TIR footprints (Figures 4c and 4f). These results indicate that on average, CTH is largest at the center and 3D radiative effects are insignificant at thermal infrared wavelengths.

In the transition zone, moving away from the cloud edges, the band 3N reflectance gradually decreases to a ("clear-sky") value of 0.30–0.31 in IM and 0.05–0.07 over the dark ocean in TO. For the two smallest cloud sizes (L = 90 m and L = 150 m), the reflectance distributions in the shadowy and illuminated transition zones are very similar and symmetric, along all directions and both in IM and TO. For the larger continental clouds in IM ($L \geq 300$ m), however, there is a marked asymmetry between the reflectance distributions in the shadowy and illuminated transition zones. While the reflectance shows little directional dependence on the illuminated side, it varies considerably with direction, and also tends to be smaller, on the shadowy side. This asymmetry is caused by the appearance of long and extensive shadows cast by these horizontally larger and vertically higher clouds. The shadowy-side reflectance always reaches its lowest value in the along-sun direction, because this azimuth samples the most shadows. In the W–E and N-S directions, the shadowy–illuminated asymmetry is less pronounced, but the shadowy-side minimum reflectance still tends to be lower than the illuminated-side minimum reflectance, because these azimuths also experience a certain degree of shadowing. In the cross-sun direction, however, the entire reflectance distribution (in-cloud and transition zone), remains remarkably symmetric to the centroid for all cloud sizes, as this azimuth is the least affected by shadowing. Apart from having lower reflectance values, the results are essentially the same in band 5.

Note that for the largest clouds, which cast the largest shadows, the reflectance in non-cross-sun directions reaches its minimum within less than 1 L to the shadowy cloud edge and starts increasing again (e.g. see Figure 4m for L = 900 m). This behavior is due to encountering the self-shadow or the shadows of neighboring clouds, as depicted for an individual case in Figures 3c and 3d.

The signature of shadows in the transition zone of TO clouds is significantly weaker and does not have a clear-cut direction dependence as for IM clouds. The ocean is generally very dark and, thus, the contrast between shadowed and illuminated areas is much smaller than over land. The magnitude of wind-induced surface reflectance variations can be larger than the darkening caused by shadows. In addition, the effect of wind can be both brightening and darkening, depending on wind speed, wind direction, and view geometry. As a result, the minimal transition zone ocean reflectance is not necessarily observed in the along-sun direction or even on the shadowy side. For the largest clouds (L = 600 m and L = 900 m), the lowest shadowy-side band 3N reflectance is encountered in the W–E direction, while the lowest reflectance in the along-sun direction is observed on the illuminated side (Figures 5j and 5m). Like in IM, however, the cross-sun reflectance distributions are the most symmetric and show the least shadowing effects for all marine cloud sizes.

The effect of shadows on surface temperature is less obvious, as the along-sun BT_{14} values in the shadowy-side transition zone are usually not the coldest; the exceptions, perhaps, are the largest cloud size bins in IM (Figures 4l and 4o). Surface temperature variations with direction, up to 3–4 K in IM and 1–2 K in TO, rather reflect geographical variations in land and sea surface properties.

3.2. Cloud Size Dependence of the Reflectance Distribution

The composited cross-sun reflectance and BT_{14}, which are the least affected by shadowing–illumination effects, are plotted in Figure 6 as a function of chord length. The band 3N and band 5 in-cloud reflectance steadily increase with cloud size in both IM and TO; however, the peak reflectance is a factor of 3–4 times larger in continental clouds than in marine clouds for all size bins. For example, the band 3N peak reflectance increases from 0.40 to 0.58 in IM and from 0.09 to 0.21 in TO between L = 90 m and L = 900 m. Because the visible reflectance increases close to linearly with optical thickness for small–medium clouds, this implies that the peak optical thickness is also about 3–4 times larger in IM clouds than in TO clouds for a given chord length. The reflectances in the IM region are sufficiently high to place them within the saturated regime, where the band 5 reflectance

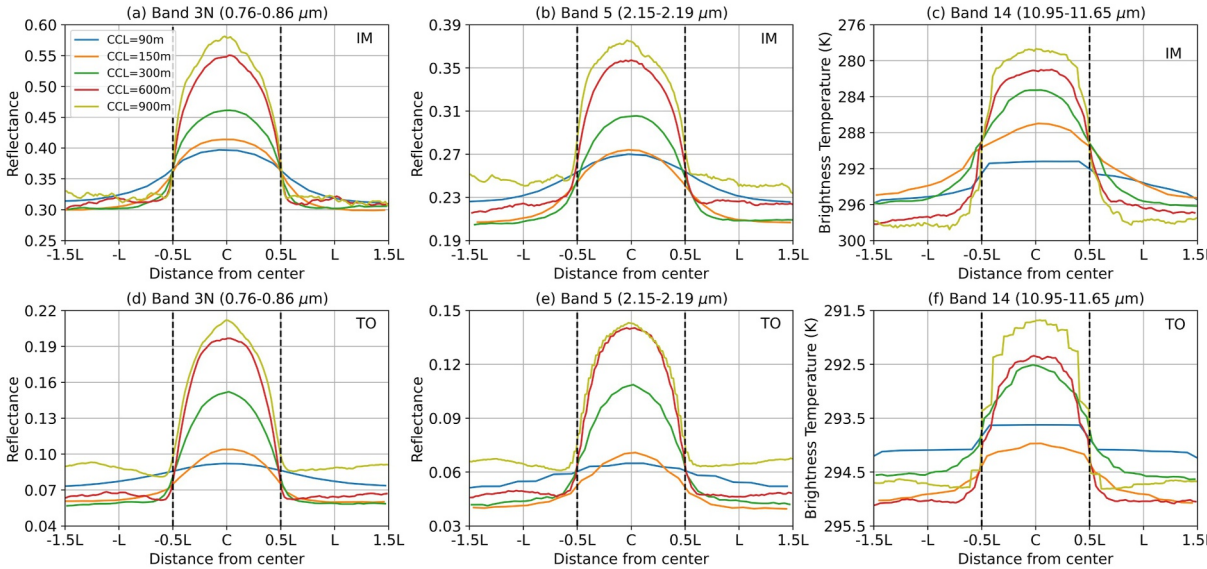

Figure 6. Composited reflectance distribution as a function of shallow cumulus chord length in band 3N (a, d) and band 5 (b, e), and brightness temperature distribution in band 14 (c, f) in the cross-sun direction for Inner Mongolia (a–c) and Tropical Ocean (d–f). Note the different *y*-axis ranges for IM and TO.

shows little dependence on optical thickness and is primarily a function of droplet effective radius (as per the lookup tables in Werner et al., 2016). Therefore, the observed increase in the band 5 peak reflectance with chord length suggests that cloud top effective radius is slightly smaller in larger IM clouds compared to their smaller counterparts. In contrast, the TO region exhibits much weaker reflectances, remaining in a region where both band 3N and band 5 reflectances increase with optical thickness. Thus, the band 5 reflectances alone cannot be used to determine how the effective radius varies with chord length in TO clouds.

Coincidentally, the minimum cloud top temperature (BT_{14}) systematically decreases with cloud size, by about 12 K (291–279 K) in IM and about 2 K (293.5–291.5 K) in TO. Assuming a lapse rate of 9 K/km in IM and 3–4 K/km in TO, this corresponds to a cloud top height increase of 1.3 km in IM and half that, 0.6 km, in TO.

Taken together, these results indicate that horizontally larger clouds are generally brighter, optically thicker, and have higher cloud tops. The liquid water path is also likely to increase with cloud size, because it is determined primarily by the optical thickness rather than the drop effective radius (Horváth et al., 2014; Seethala & Horváth, 2010). For the same chord length, however, shallow Cu is significantly thicker in IM than in TO. The increase of CTH with chord length is also twice as large in IM, likely reflecting the land–ocean difference in the maximum height of the capping inversion: up to 4 km in IM (Shi et al., 2017) and 2 km in TO (Mieslinger et al., 2019).

The band 3N minimum (baseline clear-sky) reflectance is 0.30–0.31 in the transition zone of IM clouds. The reflectance increases to 0.36–0.38 at the cloud edge (±0.5 L), showing little if any dependence on chord length. In TO, the clear-sky reflectance is 0.06–0.08, with the higher baseline observed in the largest chord length bin (L = 900 m). The reflectance increases to 0.075–0.100 at the cloud edge. In band 5, the reflectance between clear-sky and the cloud edge increases from 0.21 to 0.24 to 0.25–0.28 in IM and from 0.04 to 0.06 to 0.050–0.075 in TO, the baseline, again, being higher for the largest clouds. These observations constitute a relative reflectance increase of 20%–25% within one chord length of the cloud edge, the brightening being remarkably constant with cloud size, surface type, and wavelength.

For context, we compare our observations with previous estimates of reflectance enhancement in the transition zone. Koren et al. (2007) and Várnai and Marshak (2009) calculated the clear-sky reflectance as a function of distance from the nearest cloud, averaged over dozens of oceanic MODIS scenes. These studies analyzed larger clouds with L > 1 km, but did not classify the results by cloud size and considered the mean reflectance 20 km from the nearest cloud as the clear-sky baseline. In addition, the first 2–3 km from the cloud edge were excluded, citing detector stray light and latency effects. Koren et al. (2007) found a reflectance enhancement of 11% at

0.66 μm and 13% for 2.13 μm, between clear-sky and 3 km from the clouds. Várnai and Marshak (2009) reported an enhancement of 15%–25% at 0.86 μm and 20%–40% at 2.13 μm, between clear-sky and 2 km from the clouds. Twohy et al. (2009), on the other hand, only measured the reflectance distribution of two large shallow Cu clouds in the Indian Ocean with L = 2–3 km. Their high-resolution (30 m) aircraft observations showed a 50%–70% reflectance increase within one chord length of the cloud edge, at both 0.64 and 1.06 μm. The higher fractional increase occurred in a clean environment with a very low background aerosol load, highlighting the sensitivity of the results to the clear-sky baseline.

Considering the differences in pixel resolution as well as the sampled cloud sizes and transition zone range, our ASTER estimate of a 20%–25% average reflectance increase in the immediate vicinity of shallow Cu with L < 1 km is in the same ballpark as that of Koren et al. (2007) and Várnai and Marshak (2009). The results of Twohy et al. (2009), however, reveal that in individual cases of larger clouds, the reflectance increase can be twice as large as this mean value.

The lack of wavelength dependence in our cross-sun reflectance enhancement suggests that the observed near-field brightening is mostly due to the presence of small, evaporating cloud droplets (undetected cloud patches) and swollen hygroscopic particles in the humidity halo of clouds. 3D radiative enhancement is wavelength dependent, because Rayleigh scattering in clear areas is more effective at shorter wavelengths in redirecting cloud-scattered light into the satellite's field of view (Várnai & Marshak, 2009). Dry aerosol particles also exhibit stronger scattering at shorter wavelengths. Most importantly, aerosol and Rayleigh scattering effects are both very weak in band 5 (2.16 μm) compared to band 3N (0.82 μm). Therefore, our findings are more consistent in this regard with those of Twohy et al. (2009), who also found wavelength-independent brightening in the immediate vicinity of clouds. 3D effects, on the other hand, might be more significant at larger distances from the cloud edge, especially in the along-sun direction and on the illuminated side of optically thick clouds, as observed by Várnai and Marshak (2009).

3.2.1. The Role of Surface Temperature and Bowen Ratio

The BT_{14} distributions show that cloud chord length and cloud top height strongly depend on surface temperature, especially in IM, where land properties are geographically quite heterogeneous. The IM surface temperature, approximated roughly as the maximum BT_{14} in the transition zone, steadily increases from 295 to 299 K as cloud size increases from L = 90 m to L = 900 m. The composite-mean TO sea surface temperature (SST) varies within a much smaller range of 294–295 K; however, the generally positive correlation between SST and cloud size is still noticeable, although it is not as marked as in IM.

The interactions between shallow convection and surface properties are rather complex and fall beyond the scope of the current study. Nevertheless, our result that a warmer surface tends to trigger more vigorous shallow Cu with larger horizontal extent and higher tops is consistent with the findings of LES simulations and prior observations. Land surface heterogeneity, especially of soil moisture, can induce secondary circulations which promote vertical motion over hot and dry patches (Avissar & Liu, 1996; Lee et al., 2019). Simulations by Sakradzija and Hohenegger (2017) suggested that the cloud-base mass flux and, thus, cloud size, is primarily controlled by the Bowen ratio, the ratio of the sensible heat flux to the latent heat flux. In line with this, the ASTER-based study of marine shallow Cu by Mieslinger et al. (2019) found that CTH and the frequency of large clouds increase with increasing Bowen ratio. Most importantly, the radiosonde measurement campaign by Shi et al. (2017) revealed that the formation of Inner Mongolia shallow Cu is driven by surface forcing and favors high Bowen ratio and low soil moisture, that is, high sensible heat flux and low latent heat flux. Bowen ratio, in turn, increases with surface temperature, particularly in a relatively dry environment such as the IM grasslands (Lin et al., 2022).

3.3. Cloud Size Dependence of the Transition Zone

To better elucidate the variation of the transition zone size with cloud chord length, we normalize the cross-sun curves plotted in Figure 6 by subtracting the minimum value from the reflectance and the maximum value from BT_{14}, and then dividing by the amplitude (maximum minus minimum), similar to Gu et al. (2021). The resulting normalized composites are depicted in Figure 7. As shown, the decrease of the normalized reflectance with normalized distance is much steeper for larger clouds. Consequently, the relative (chord length-normalized) extent of the transition zone decreases steadily with increasing cloud size in both bands and geographic regions.

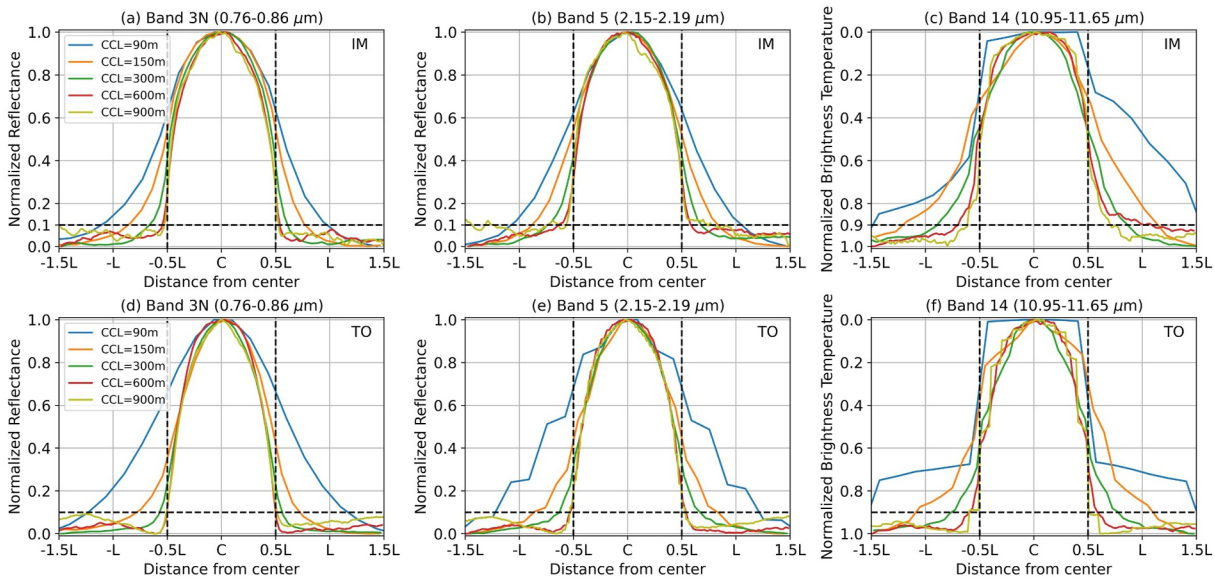

Figure 7. Normalized composited reflectance distribution in band 3N (a, d) and band 5 (b, e), and brightness temperature distribution in band 14 (c, f) in the cross-sun direction for Inner Mongolia (a–c) and Tropical Ocean (d–f).

For a quantitative measure of the transition zone size, we use the nearest distance from cloud edge at which the normalized reflectance (or BT_{14}) drops to 0.1, that is, 10% of its in-cloud maximum (or minimum), summarized in Tables 2–4. Borrowing from signal processing terminology, this parameter is the half-width at one-tenth-maximum minus the cloud radius. This definition reduces the ambiguity arising from the noisy part of the curves, where reflectance does not smoothly decrease with distance. The metric does not necessarily capture the full transition zone, but allows a convenient characterization of the chord length dependence of the observed near-field halo and its comparison with Gu et al.'s (2021, 2024) LES results. For the subset of clouds where reflectance and BT reach a plateau, one could estimate a generally larger asymptotic halo size (see Appendix A).

For IM clouds, the band 3N transition zone size decreases from 0.6 to 0.05 L between L = 90 m and L = 900 m (Table 2). For TO clouds, the transition zone size decreases from 0.7 L to practically zero between the smallest and largest clouds, when using the 0.1 normalized reflectance threshold. A slightly smaller threshold would result in larger and non-zero transition zone sizes for all cloud chord bins. The results are very similar in band 5, the transition zone size decreases from 0.6 to 0.08 L in IM and from 0.7 to 0.03 L in TO, as chord length increases (Table 3). Due to the less steep decrease of the band 5 normalized reflectance, the transition zone sizes are slightly larger than in band 3N and are non-zero even for the largest TO clouds at the 0.1 threshold.

The BT_{14} relative transition zone size also shows a steady decrease with chord length; however, it is noticeably larger than the reflectance transition zones for all cloud sizes, decreasing from 1 to 0.1 L in IM and from 1 to 0.08 L in TO, between the smallest and the largest clouds (Table 4). The larger transition zone at thermal infrared wavelengths is likely due to the water vapor sensitivity of the infrared window channels and the strongly non-linear dependence of reflectance on RH. The scattering cross section of hygroscopic particles drops very sharply between saturation and RH = 90% and then slowly decreases toward the background value for lower RH values (Twohy et al., 2009). Therefore, at larger distances from the cloud edge, humidity can be elevated enough to affect the TIR channels, but too small to measurably increase the size and scattering of hygroscopic particles. These observations imply that the humidity halo of clouds is generally larger than their reflectance halo.

Table 2
The Normalized and Absolute Size of Transition Zone in Band 3N

	Inner Mongolia		Tropical Ocean	
	Left side	Right side	Left side	Right side
90 m	0.6 L (54 m)	0.5 L (45 m)	0.75 L (67.5 m)	0.7 L (63 m)
150 m	0.35 L (52.5 m)	0.3 L (45 m)	0.25 L (37.5 m)	0.3 L (45 m)
300 m	0.2 L (60 m)	0.15 L (45 m)	0.1 L (30 m)	0.05 L (15 m)
600 m	0.05 L (30 m)	0.05 L (30 m)	–	–
900 m	0.05 L (45 m)	0.05 L (45 m)	–	–

The decrease in the relative size of the radiative transition zone with increasing chord length agrees well with the LES results of Gu et al. (2021, 2024). They found that the distribution of RH and liquid water content in and

Table 3
The Normalized and Absolute Size of Transition Zone in Band 5

	Inner Mongolia		Tropical Ocean	
	Left side	Right side	Left side	Right side
90 m	0.6 L (54 m)	0.55 L (50 m)	0.7 L (63 m)	0.7 L (63 m)
150 m	0.4 L (60 m)	0.35 L (52.5 m)	0.4 L (60 m)	0.3 L (45 m)
300 m	0.25 L (75 m)	0.2 L (60 m)	0.1 L (30 m)	0.15 L (45 m)
600 m	0.1 L (60 m)	0.1 L (60 m)	0.06 L (36 m)	0.09 L (54 m)
900 m	0.08 L (72 m)	0.25 L (225 m)	0.03 L (27 m)	0.03 L (27 m)

around modeled clouds has a bell shape and shows the same chord size dependence as our satellite observations. The distributions of vertical velocity, potential temperature, and turbulent kinetic energy, on the other hand, have more complex shapes with multiple minima or maxima. Although the radiation field of clouds and their environment is controlled by more complex factors in the real atmosphere, our results indicate that in an LES context, reflectance and brightness temperature are first-order proxies for liquid water amount and humidity.

According to our analysis summarized in Figure 8 and Tables 2–4, the absolute size of the reflectance halo is typically 50–100 m, depending on band, while that of the BT_{14} halo is slightly larger, 60–180 m. Based on a spatial autocorrelation analysis of modeled liquid water and RH, Gu et al. (2024) estimate a typical moist halo size of 100–150 m for clouds with chord lengths between 200 and 1,000 m. Note that Gu et al. (2024) report equivalent halo diameters of 200–300 m, which must be halved to be compatible with our measure of the transition zone size. Therefore, the modeled moist halo is somewhat larger than the observed reflectance halo but compares well with the BT_{14} halo; the better agreement with the latter is not completely surprising, because the infrared window channels, unlike the reflectance channels, are sensitive not only to cloud and aerosol particles but also to water vapor. We also note that in the simulations, the moist halo size is largest at cloud base and decreases upwards. Our passive satellite observations cannot resolve vertical variations and are representative of the cloud base.

Overall, the decrease of the relative halo size with increasing chord length indicates that the absolute halo size does not scale linearly with cloud size. This feature of the observed radiative halos holds over both land and ocean, suggesting that size-independent length scales are responsible for the halo formation around shallow cumulus, in agreement with Gu et al.'s (2021, 2024) findings for LES moist halos.

4. Summary and Conclusions

We analyzed the ASTER-observed reflectance and brightness temperature distribution of shallow cumulus and its near field in the Inner Mongolia grasslands and Tropical Ocean, as a function of horizontal cloud size. The 15-m-resolution imagery allowed capturing smaller scale clouds, which are beyond the reach of medium-resolution sensors, such as MODIS, used in prior studies. The 1D reflectance curves, composited along cloud transects, show varying degrees of shadowing–illumination effects, depending on cloud size and slice direction. The cross-sun reflectance distributions, which are least affected by shadowing–illumination effects, exhibit a symmetric, bell-shaped decrease from the cloud center to the cloud edges and into the transition zone. The modeled distribution of RH and liquid water content, parameters primarily affecting reflectance and BT, show a similar bell-shaped variation in LES shallow cumulus and their environs (Gu et al., 2021, 2024), in agreement with our observations.

A notable feature is that the peak reflectance of clouds with $L \geq 300$ m is slightly shifted from the cloud center in all, but the cross-sun transects. The shift in the peak reflectance's location is always to the illuminated side in continental clouds, but it can be to the shadowed side in the largest oceanic clouds. This off-center shift can be explained by the competition between two 3D effects: (a) radiative smoothing caused by horizontal variations in the volume extinction coefficient and (b) radiative sharpening due to CTH variations (Várnai, 2000). The observations indicate that CTH variations and, thus, radiative sharpening, are more prominent in continental clouds than in oceanic clouds.

Table 4
The Normalized and Absolute Size of Transition Zone in Band 14

	Inner Mongolia		Tropical Ocean	
	Left side	Right side	Left side	Right side
90 m	>1 L (90 m)	>1 L (90 m)	>1 L (90 m)	>1 L (90 m)
150 m	0.75 L (67.5 m)	0.7 L (63 m)	0.6 L (90 m)	0.6 L (90 m)
300 m	0.4 L (120 m)	0.35 L (105 m)	0.3 L (90 m)	0.25 L (75 m)
600 m	0.2 L (120 m)	0.5 L (300 m)	0.1 L (60 m)	0.1 L (60 m)
900 m	0.1 L (90 m)	0.2 L (180 m)	0.08 L (72 m)	–

The composited reflectance and BT curves reveal that cloud brightness, optical thickness, and top height steadily increase with increasing chord length in both study regions. Inner Mongolia clouds of a given chord length, however, are 3–4 times brighter and optically thicker than their oceanic counterparts. In addition, continental clouds are systematically larger and have higher tops at warmer surface temperatures, suggesting that convection is more vigorous over warm and dry land patches characterized by high Bowen ratios.

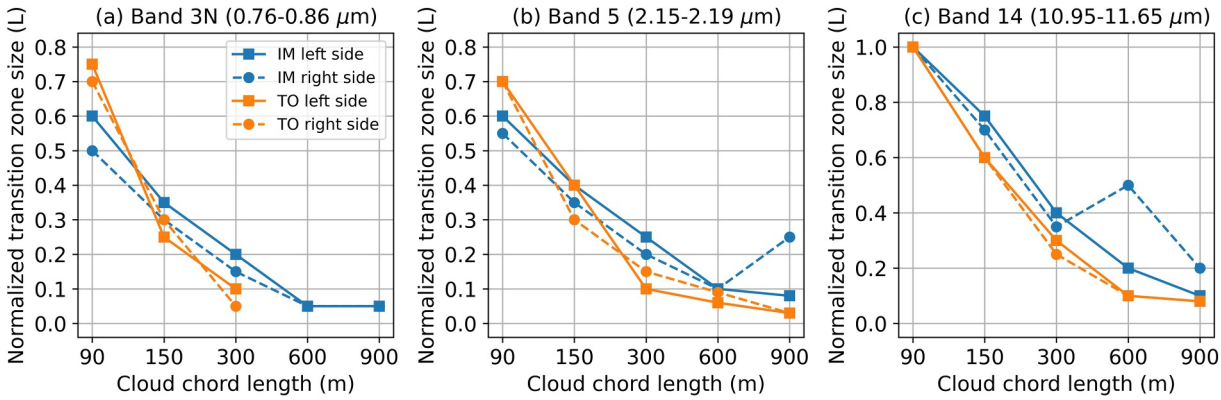

Figure 8. The normalized left- and right-side halo size as a function of cloud chord length in (a) band 3N, (b) band 5, and (c) band 14, separately for IM and TO. Note the different *y*-axis range in panel (c).

Reflectance increases by 20%–25% above its clear-sky value within one chord length of the cloud edge and this increase shows little variation with cloud size, region, or wavelength. These results imply that the brightening in the near-cloud transition zone is caused primarily by hygroscopically-swollen aerosols and undetected cloud patches rather than 3D effects or increased dry aerosol scattering, which are wavelength dependent.

The size of the transition zone was quantitatively characterized by the distance from cloud edge at which the cloud's radiative perturbation (i.e., the reflectance increase or brightness temperature decrease compared to the clear-sky baseline) dropped to 10% of its maximum value near the cloud center. The relative (chord length-normalized) size of both the reflectance and the brightness temperature transition zone steadily decreases with increasing cloud size; that is, the absolute size of the halo region does not scale linearly with cloud size. We note that the relative size of the moist halo around simulated shallow cumulus also systematically decreases with increasing cloud size (Gu et al., 2021, 2024), consistent with our observations.

The brightness temperature transition zone, however, tends to be a bit larger than the reflectance transition zone, likely due to the larger sensitivity of the infrared channels to water vapor. The absolute size of the reflectance halo is 50–100 m, while that of the brightness temperature halo is 60–180 m by our observational metric. The latter compares well with the 100–150 m moist halo size found in the simulations of Gu et al. (2024) using a spatial autocorrelation metric.

Overall, our observations indicate that the latest LES models generate shallow cumulus fields which are realistic in the characteristics of the humidity halo surrounding the clouds. The consistent modeling and observational results also suggest with some confidence that halo formation is governed by processes with size-independent length scales. Future work can further refine the properties of the radiative halo by extending the analysis to 2D (all azimuth directions) and exploiting even higher resolution imagery (up to 3 m) offered by new generation satellite constellations such as Planet.

Appendix A

For Inner Mongolia clouds with L $\leq$ 300 m, the reflectance and brightness temperature smoothly decrease and increase with distance and then plateau. For this subset, we could extend the analysis range to $\pm$2L and define an asymptotic transition zone size metric as the distance between the cloud edge and the lowest reflectance or highest brightness temperature, listed in Table A1. The magnitude of the asymptotic size metric for clouds with L = 90 and 150 m is about or slightly over 1 L, that is, comparable to the size of clouds. However, the asymptotic transition zone size of clouds with L = 300 m, varying between 0.5 and 0.8 L, is smaller than the cloud size. Consistent with the size metric defined in Section 3.3, the asymptotic transition zone metric also has a larger normalized size in smaller clouds, but larger clouds have a larger absolute size. For example, the asymptotic transition zone size in band 5 is 1.2 L (108 m), 0.9 L (135 m), and 0.6 L (180 m) for L = 90 m, 150 m, and 300 m, respectively.

Table A1
The Normalized and Absolute Size of the Asymptotic Transition Zone Metric for IM Clouds With $L \leq 300$ m

	Band 3N		Band 5		Band 14	
	Left side	Right side	Left side	Right side	Left side	Right side
90 m	1.2 L (108 m)	1.1 L (99 m)	1.2 L (108 m)	1.2 L (108 m)	1.5 L (135 m)	1.3 L (117 m)
150 m	1 L (150 m)	0.7 L (105 m)	0.9 L (135 m)	0.8 L (120 m)	1.1 L (165 m)	1 L (150 m)
300 m	0.5 L (150 m)	0.4 L (120 m)	0.6 L (180 m)	0.5 L (150 m)	0.8 L (240 m)	0.8 L (240 m)

Conflict of Interest

The authors declare no conflicts of interest relevant to this study.

Data Availability Statement

ASTER L1B radiance data are publicly accessible through NASA (2001). The Python functions implemented for calculating marine cloud field statistics are freely available in the python package *typhon*, subpackage *cloudmask* (Mieslinger et al., 2019).

Acknowledgments
This work was supported by the National Natural Science Foundation of China (Grants 42205147 and U2442214). This work also contributes to EXC 2037 "CLICCS – Climate, Climatic Change, and Society" – project number: 390683824, funded by the Deutsche Forschungsgemeinschaft (DFG, German Research Foundation) under Germany's Excellence Strategy, and to ESRAH (Earth and Society Research Hub) at University of Hamburg. Mengqi Liu would like to thank Theresa Mieslinger for her previous research and Oliver Lemke for software support. The detailed and constructive suggestions of three anonymous reviewers greatly improved the paper. Open Access funding enabled and organized by Projekt DEAL.

References

Abrams, M., Hook, S., & Ramachandran, B. (2000). *ASTER user handbook*, *Advanced Thermal Emission and Reflection Radiometer*. NASA JPL. Retrieved from https://asterweb.jpl.nasa.gov/content/03_data/04_Documents/aster_user_guide_v2.pdf

Avissar, R., & Liu, Y. (1996). Three-dimensional numerical study of shallow convective clouds and precipitation induced by land surface forcing. *Journal of Geophysical Research*, *101*(D3), 7499–7518. https://doi.org/10.1029/95JD03031

Baum, B. A., Menzel, W. P., Frey, R. A., Tobin, D. C., Holz, R. E., Ackerman, S. A., et al. (2012). MODIS cloud-top property refinements for Collection 6. *Journal of Applied Meteorology and Climatology*, *51*(6), 1145–1163. https://doi.org/10.1175/JAMC-D-11-0203.1

Charlson, R. J., Ackerman, A. S., Bender, F. A.-M., Anderson, T. L., & Liu, Z. (2007). On the climate forcing consequences of the albedo continuum between cloudy and clear air. *Tellus B*, *59*(4), 715–727. https://doi.org/10.1111/j.1600-0889.2007.00297.x

De Vera, M. V., Di Girolamo, L., Zhao, G., Rauber, R. M., Nesbitt, S. W., & McFarquhar, G. M. (2024). Observations of the macrophysical properties of cumulus cloud fields over the tropical western Pacific and their connection to meteorological variables. *Atmospheric Chemistry and Physics*, *24*(9), 5603–5623. https://doi.org/10.5194/acp-24-5603-2024

Eytan, E., Gristey, J. J., & Feingold, G. (2025). The net radiative effect of the ill-defined clear-sky in the vicinity of clouds. *AGU Advances*, *6*(1), e2024AV001407. https://doi.org/10.1029/2024AV001407

Govender, M., Chetty, K., & Bulcock, H. (2007). A review of hyperspectral remote sensing and its application in vegetation and water resource studies. *Water SA*, *33*(2). https://doi.org/10.4314/wsa.v33i2.49049

Griewank, P. J., Heus, T., Lareau, N. P., & Neggers, R. A. J. (2020). Size dependence in chord characteristics from simulated and observed continental shallow cumulus. *Atmospheric Chemistry and Physics*, *20*(17), 10211–10230. https://doi.org/10.5194/acp-20-10211-2020

Gu, J. F., Plant, R. S., Holloway, C. E., & Clark, P. A. (2024). The moist halo region around shallow cumulus clouds in large eddy simulations. *Quarterly Journal of the Royal Meteorological Society*, *150*(760), 1501–1517. https://doi.org/10.1002/qj.4656

Gu, J.-F., Plant, R. S., Holloway, C. E., & Jones, T. R. (2021). Composited structure of non-precipitating shallow cumulus clouds. *Quarterly Journal of the Royal Meteorological Society*, *147*(738), 2818–2833. https://doi.org/10.1002/qj.4101

Guillaume, A., Kahn, B. H., Yue, Q., Fetzer, E. J., Wong, S., Manipon, G. J., et al. (2018). Horizontal and vertical scaling of cloud geometry inferred from CloudSat data. *Journal of the Atmospheric Sciences*, *75*(7), 2187–2197. https://doi.org/10.1175/JAS-D-17-0111.1

Horváth, Á., Carr, J. L., Girina, O. A., Wu, D. L., Bril, A. A., Mazurov, A. A., et al. (2021). Geometric estimation of volcanic eruption column height from GOES-R near-limb imagery – Part 1: Methodology. *Atmospheric Chemistry and Physics*, *21*, 12189–12206. https://doi.org/10.5194/acp-21-12189-2021

Horváth, Á., Seethala, C., & Deneke, H. (2014). View angle dependence of MODIS liquid water path retrievals in warm oceanic clouds. *Journal of Geophysical Research: Atmospheres*, *119*(13), 8304–8328. https://doi.org/10.1002/2013JD021355

Hulley, G. C., & Hook, S. J. (2008). A new methodology for cloud detection and classification with ASTER data. *Geophysical Research Letters*, *35*(16), L16812. https://doi.org/10.1029/2008GL034644

Koren, I., Remer, L. A., Kaufman, Y. J., Rudich, Y., & Martins, J. V. (2007). On the twilight zone between clouds and aerosols. *Geophysical Research Letters*, *34*(8), L08805. https://doi.org/10.1029/2007GL029253

Lee, J. M., Zhang, Y., & Klein, S. A. (2019). The effect of land surface heterogeneity and background wind on shallow cumulus clouds and the transition to deeper convection. *Journal of the Atmospheric Sciences*, *76*(2), 401–419. https://doi.org/10.1175/JAS-D-18-0196.1

Lin, H., Li, Y., & Zhao, L. (2022). Partitioning of sensible and latent heat fluxes in different vegetation types and their spatiotemporal variations based on 203 FLUXNET sites. *Journal of Geophysical Research: Atmospheres*, *127*(21), e2022JD037142. https://doi.org/10.1029/2022JD037142

Mieslinger, T., Horváth, Á., Buehler, S. A., & Sakradzija, M. (2019). The dependence of shallow cumulus macrophysical properties on large-scale meteorology as observed in ASTER imagery. *Journal of Geophysical Research: Atmospheres*, *124*(21), 11477–11505. https://doi.org/10.1029/2019JD030768

Mieslinger, T., Stevens, B., Kölling, T., Brath, M., Wirth, M., & Buehler, S. A. (2022). Optically thin clouds in the trades. *Atmospheric Chemistry and Physics*, *22*(10), 6879–6898. https://doi.org/10.5194/acp-22-6879-2022

NASA/METI/AIST/Japan Spacesystems and U.S./Japan ASTER Science Team. (2001). ASTER level 1B data set registered radiance at the sensor [Dataset]. *NASA Land Processes Distributed Active Archive Center*. https://doi.org/10.5067/ASTER/AST_L1B.003

Perry, K. D., & Hobbs, P. V. (1996). Influences of isolated cumulus clouds on the humidity of their surroundings. *Journal of the Atmospheric Sciences*, *53*(1), 159–174. https://doi.org/10.1175/1520-0469(1996)053<0159:IOICCO>2.0.CO;2

Radke, L. F., & Hobbs, P. V. (1991). Humidity and particle fields around some small cumulus clouds. *Journal of the Atmospheric Sciences*, *48*(9), 1190–1193. https://doi.org/10.1175/1520-0469(1991)048<1190:HAPFAS>2.0.CO;2

Sakradzija, M., & Hohenegger, C. (2017). What determines the distribution of shallow convective mass flux through a cloud base? *Journal of the Atmospheric Sciences*, *74*(8), 2615–2632. https://doi.org/10.1175/JAS-D-16-0326.1

Seethala, C., & Horváth, Á. (2010). Global assessment of AMSR-E and MODIS cloud liquid water path retrievals in warm oceanic clouds. *Journal of Geophysical Research*, *115*(D13), D13202. https://doi.org/10.1029/2009JD012662

Shi, H., Chen, H., Xia, X. A., Fan, X., Zhang, J., Li, J., & Ling, C. (2017). Intensive radiosonde measurements of summertime convection over the Inner Mongolia grassland in 2014: Difference between shallow cumulus and other conditions. *Advances in Atmospheric Sciences*, *34*(6), 783–790. https://doi.org/10.1007/s00376-017-6284-2

Tackett, J. L., & Di Girolamo, L. (2009). Enhanced aerosol backscatter adjacent to tropical trade wind clouds revealed by satellite-based LiDAR. *Geophysical Research Letters*, *36*(14), L14804. https://doi.org/10.1029/2009gl039264

Twohy, C. H., Coakley, J. A., Jr., & Tahnk, W. R. (2009). Effect of changes in relative humidity on aerosol scattering near clouds. *Journal of Geophysical Research*, *114*(D5), D05205. https://doi.org/10.1029/2008JD010991

Várnai, T. (2000). Influence of three-dimensional radiative effects on the spatial distribution of shortwave cloud reflection. *Journal of the Atmospheric Sciences*, *57*(2), 216–229. https://doi.org/10.1175/1520-0469(2000)057<0216:IOTDRE>2.0.CO;2

Várnai, T., & Davies, R. (1999). Effects of cloud heterogeneities on shortwave radiation: Comparison of cloud-top variability and internal heterogeneity. *Journal of the Atmospheric Sciences*, *56*(24), 4206–4224. https://doi.org/10.1175/1520-0469(1999)056<4206:EOCHOS>2.0.CO;2

Várnai, T., & Marshak, A. (2002). Observations of three-dimensional radiative effects that influence MODIS cloud optical thickness retrievals. *Journal of the Atmospheric Sciences*, *59*(9), 1607–1618. https://doi.org/10.1175/1520-0469(2002)059<1607:OOTDRE>2.0.CO;2

Várnai, T., & Marshak, A. (2009). MODIS observations of enhanced clear sky reflectance near clouds. *Geophysical Research Letters*, *36*(6), L06807. https://doi.org/10.1029/2008GL037089

Várnai, T., & Marshak, A. (2011). Global CALIPSO observations of aerosol changes near clouds. *IEEE Geoscience and Remote Sensing Letters*, *8*, 19–23. https://doi.org/10.1109/LGRS.2010.2049982

Werner, F., Wind, G., Zhang, Z., Platnick, S., Di Girolamo, L., Zhao, G., & Meyer, K. (2016). Marine boundary layer cloud property retrievals from high-resolution ASTER observations: Case studies and comparison with Terra MODIS. *Atmospheric Measurement Techniques Discussions*, *9*(12), 5869–5894. https://doi.org/10.5194/amt-2016-265

Yamaguchi, Y., Kahle, A. B., Tsu, H., Kawakami, T., & Pniel, M. (1998). Overview of advanced spaceborne thermal emission and reflection radiometer (ASTER). *IEEE Transactions on Geoscience and Remote Sensing*, *36*(4), 1062–1071. https://doi.org/10.1109/36.700991

Zhao, G., & Di Girolamo, L. (2006). Cloud fraction errors for trade wind cumuli from EOS-Terra instruments. *Geophysical Research Letters*, *33*(20), L20802. https://doi.org/10.1029/2006gl027088

Zhao, G., & Di Girolamo, L. (2007). Statistics on the macrophysical properties of trade wind cumuli over the tropical western Atlantic. *Journal of Geophysical Research*, *112*(D10), D10204. https://doi.org/10.1029/2006JD007371